Colloidal Bismuth Nanocrystals as a Model Anode Material for Rechargeable Mg-Ion Batteries: Atomistic and Mesoscale Insights

*Kostiantyn V. Kravchyk, [1,2] Laura Piveteau, [1,2] Riccarda Caputo, [1** Meng He, [1,2] Nicholas P. Stadie, [1,2*** Maryna I. Bodnarchuk, [2] Rainer T. Lechner, [3] and Maksym V. Kovalenko[1,2*]*

[1] Department of Chemistry and Applied Biosciences, ETH Zürich, Vladimir-Prelog-Weg 1, Zurich, CH-8093, Switzerland.

[2] Empa-Swiss Federal Laboratories for Materials Science and Technology, Überlandstrasse 129, Dübendorf, CH-8600, Switzerland.

[3] Institute of Physics, Montanuniversitaet Leoben, Franz-Josef-Strasse 18, A-8700 Leoben, Austria.

[*] Email: mvkovalenko@ethz.ch.

[**] Current address: ICQMS, International Centre for Quantum and Molecular Structures, Department of Physics, Shanghai University, China.

[***] Current address: Department of Chemistry and Biochemistry, Montana State University, Bozeman, Montana, 59717, USA.

ABSTRACT

At present, the technical progress of secondary batteries employing metallic magnesium as the anode material has been severely hindered due to the low oxidation stability of state-of-the-art Mg electrolytes, which cannot be used to explore high voltage (> 3 V vs. Mg^{2+}/Mg) cathode materials. All known electrolytes based on oxidatively stable solvents and salts, such as $Mg(ClO_4)_2$ and Mg bis(trifluoromethanesulfonimide) react with the metallic magnesium anode, forming a passivating layer at its surface and preventing the reversible plating/stripping of Mg. Therefore, in a near-term effort to extend the upper voltage limit in the exploration of future candidate Mg-ion battery cathode materials, bismuth anodes have attracted considerable attention owing to their efficient magnesiation/de-magnesiation alloying reaction in such electrolytes. In this context, we present colloidal Bi nanocrystals (NCs) as a model anode material for the exploration of cathode materials for rechargeable Mg-ion batteries. Bi NCs demonstrate a stable capacity of 325 mAh g^{-1} over at least 150 cycles at a current density of 770 mA g^{-1}, which is among the most stable performance of Mg-ion battery anode materials. First-principles crystal structure prediction methodologies and e*x-situ* X-ray diffraction measurements reveal that the magnesiation of Bi NCs leads to the simultaneous formation of the low-temperature trigonal structure, α-Mg_3Bi_2, and the high-temperature cubic structure, β-Mg_3Bi_2, which shed insight into the high stability of this reversible alloying reaction. Furthermore, small-angle X-ray scattering measurements indicate that although the monodisperse, crystalline nature of the Bi NCs is indeed disturbed during the first discharge step, no notable morphological or structural changes occur in the following electrochemical cycles. The cost-effective and facile synthesis of colloidal Bi NCs and their remarkably high electrochemical stability upon

magnesiation make them an excellent model anode material to accelerate progress in the field of

Mg-ion secondary batteries.

In recent years, investigations of electrode materials for rechargeable metal-ion batteries (*e.g.*, Li-ion and emerging Na-ion batteries) have increasingly involved nanomaterials. In particular, monodisperse inorganic nanocrystals (NCs) and nanoparticles (NPs) of electrode materials are increasingly employed as well-defined model systems for controlling and studying the effects of particle size, composition, and morphology on electrochemical characteristics during battery operation (*e.g.*, rate capability, cycling performance, *etc.*). Such model systems are also of interest for the effective nanoscale intermixing of active electrode materials with other components,[1-8] typically also benefitting from their convenient solution-based handling. Due to very short internal diffusion paths, nanoscale materials are far less limited by their ionic and electronic conductivities than their bulk counterparts.[9-17] Nanomaterials can also withstand much greater mechanical deformation during charge/discharge cycling, a problem facing all anode materials that operate *via* alloying with either Li (such as Si, Sn, Sb, and Ge) or Na (such as Sn, Sb, and P) which is accompanied by large volumetric expansion (*e.g.*, 100-400%).[3, 18-37] Overall, these favorable attributes of nanomaterial-based electrodes have allowed the variety of inorganic compounds that can be explored as reversible Li- and Na-ion storage media to significantly widen, at least in a laboratory setting. Although the cost and complexity of the synthesis of such nanomaterials can be commercially prohibitive, the insights gained from investigating such precisely tunable model systems can guide the development of economic production routes or definitively determine whether certain materials should be pursued at all.

Herein we apply the utility of monodisperse metallic NCs as model electrode materials to the investigation of Mg-ion batteries. Secondary batteries based on magnesium arise as a result of a fundamental shortcoming of Li- and Na-ion batteries in that neither metallic lithium nor sodium – the densest and conceptually simplest sources of Li- and Na-ions – can safely be employed as

the negative electrode material (anode) in their corresponding metal-ion batteries.[38-41] The well-known reason for this is the formation of dendrites during cycling and the associated risks of electrical short-circuit and runaway exothermic reactions, in addition to the highly pyrophoric nature of these metals. Graphite is the most common anode in commercial Li-ion batteries, exhibiting a similar voltage profile to lithium metal but with a 10-fold lower charge-storage capacity. In conceptually analogous Mg-ion batteries (MIBs), on the other hand, metallic magnesium can in fact be employed as a safe and high capacity anode material,[42-47] exhibiting both dendrite-free electroplating and lower pyrophoricity. Further, concerns regarding the future security of the supply of lithium and its geographically heterogeneous natural occurrence[48] are not faced by magnesium, making MIBs an attractive alternative for large scale stationary energy storage applications; Mg is highly abundant in the Earth's crust (2.3 wt.%, ~1100 times higher than Li)[49] and extremely inexpensive (3.1 USD kg^{-1}, ~20 times lower than Li). Importantly, as a pure elemental anode material, metallic magnesium exhibits volumetric and gravimetric capacities (3833 mAh cm^{-3} and 2205 mAh g^{-1}, respectively) that are comparable to metallic lithium (2062 mAh cm^{-3} and 3861 mAh g^{-1}, respectively) and sodium (1128 mAh cm^{-3} and 1166 mAh g^{-1}, respectively) at a relatively low standard electrode potential (0.69 V vs. Li^+/Li or 0.35 V vs. Na^+/Na).[42,43,50-51] Lastly, the issue of irreversible capacity loss as a result of the formation of a solid-electrolyte interface (SEI, arising from the reduction of the electrolyte at low anodic potentials), which is a significant complexity facing a large number of Li-ion and Na-ion anode materials, is not an important issue for MIBs.

Secondary MIBs, nevertheless, face several obstacles to overcome before practical deployment will be possible, primarily with respect to significant electrochemical incompatibilities between the currently identified candidate anode, electrolyte, and cathode materials. While Mg^{2+} ions

have a similar radius to Li$^+$ ions, their bivalent charge causes strong Coulomb interactions within typical polar solid-state conductors, leading to orders of magnitude lower diffusivity and issues with respect to the electrolyte chemistry.[42,43,46,52-57] Electrolytes which are favored for their ability to reversibly strip and deposit Mg^{2+} ions on a metallic magnesium anode are typically highly reducing compounds themselves or contain such solvents, invariantly causing undesirable oxidation at the cathode and therefore restricting practical operation to within 2-3.0 V *vs.* Mg^{2+}/Mg.[42,58-62] This obstacle is faced by all studies of cathode materials for MIBs[42-44,46,47, 53,55-57,61-82] and, as a result, Chevrel-phase Mo$_6$S$_8$ has remained the benchmark cathode material for MIBs despite its modest gravimetric capacity (typically measured to be 80-100 mAh g^{-1}, with a theoretical limit of 128 mAh g^{-1}).[45] At the same time, low-cost, conventional electrolytes based on oxidatively stable salts (*e.g.*, Mg(ClO$_4$)$_2$, Mg bis(trifluoromethanesulfonimide) (Mg(TFSI)$_2$), *etc.*) in an appropriate solvent (*e.g.*, acetonitrile or various ionic liquids) cannot be used together with a metallic magnesium anode due to the irreversible deposition/stripping of Mg^{+2} and the formation of an insulating passivation layer (in contrast to the formation of a conductive SEI in Li-ion batteries).[46,54,75,83]

While the very concept of the Mg-ion battery is founded on the eventual use of metallic magnesium as the anode material, it would be of great interest for basic research purposes to establish a model anode material that is stable at higher voltages and fast enough to enable a broader search for suitable electrolytes and cathode materials. Such a high-capacity model Mg-ion anode material could be chosen from several elements which readily alloy with Mg and their multinary compounds by electrochemical means at room temperature. Numerous recent studies have been devoted to Bi,[84-94] Sb,[86] Sn,[17,95-96] Pb,[97] In,[98] Sb$_{1-x}$Bi$_x$,[99] InBi,[100] and β-SnSb,[101,102] all seeking an understanding of the electrochemical behavior of these electrode materials, the

atomistic details of ion insertion and de-insertion, and the mesoscale evolution of the electrode during cycling. Bismuth serves as an especially simple model material since it electrochemically alloys with Mg at room temperature, forming Mg_3Bi_2. While the gravimetric charge-storage capacity of Bi is an order of magnitude lower than that of metallic Mg, the theoretical volumetric charge-storage capacity of Bi (3783 mAh cm^{-3}) compares very favorably with metallic Mg (3833 mAh cm^{-3}), in addition to metallic Li (2062 mAh cm^{-3}) and Na (1128 mAh cm^{-3}). The gravimetric charge-storage capacity of Bi is, in any case, not a limiting factor to the overall energy storage capacity of full MIB cells at the present time due to the much lower capacity of available cathode materials. Altogether, bismuth is therefore an optimal model anode for future research in the field of complete Mg-ion battery systems.

Herein we report the synthesis and electrochemical characterization of monodisperse colloidal Bi NCs as an ideal model anode material for MIBs in the laboratory setting. We present atomistic and mesoscale studies of the magnesiation of bismuth by a combining first-principles calculations and experimental studies of monodisperse colloidal Bi NCs. Density functional theory (DFT) methodologies were employed to predict the thermodynamically stable crystalline phases in the Mg-Bi system. The simulated X-ray powder diffraction patterns of the relevant Mg_xBi phases were then compared to the measured diffraction patterns of *ex-situ* measured samples of Bi NCs at various stages during electrochemical discharge/charge cycling, including samples collected after 100 cycles. The evolution of the mesoscale morphology of the as-prepared Bi NC anodes during electrochemical cycling was then assessed *via* small-angle X-ray scattering (SAXS) techniques. Together, these results lead to a more complete understanding of the electrochemical cycling behavior of Bi NC anodes, enabling future methodological studies of

the integration of anode, electrolyte, and cathode toward next-generation Li- and Na-free battery concepts.

RESULTS AND DISCUSSION

Atomistic Insights into the Magnesiation of Bi. By combining crystal structure prediction methodologies and total energy DFT calculations, as detailed in the Methods section, the insertion of Mg into elemental Bi was found to take place through an alloying mechanism, leading to the co-formation of two stable phases (see Figures 1a, S1 and S2, and Table S1). These two phases comprise the commonly observed low-energy trigonal structure, α-Mg_3Bi_2,[103] and the higher energy cubic structure, β-Mg_3Bi. Experimentally, the trigonal structure is typically observed at ambient temperature and the cubic structure is stable above 976 K.[103] To the best of our knowledge, the crystal structure of β-Mg_3Bi_2 has not previously been characterized experimentally, although it has been suggested to have the Mg_3As_2 structure type.[104]
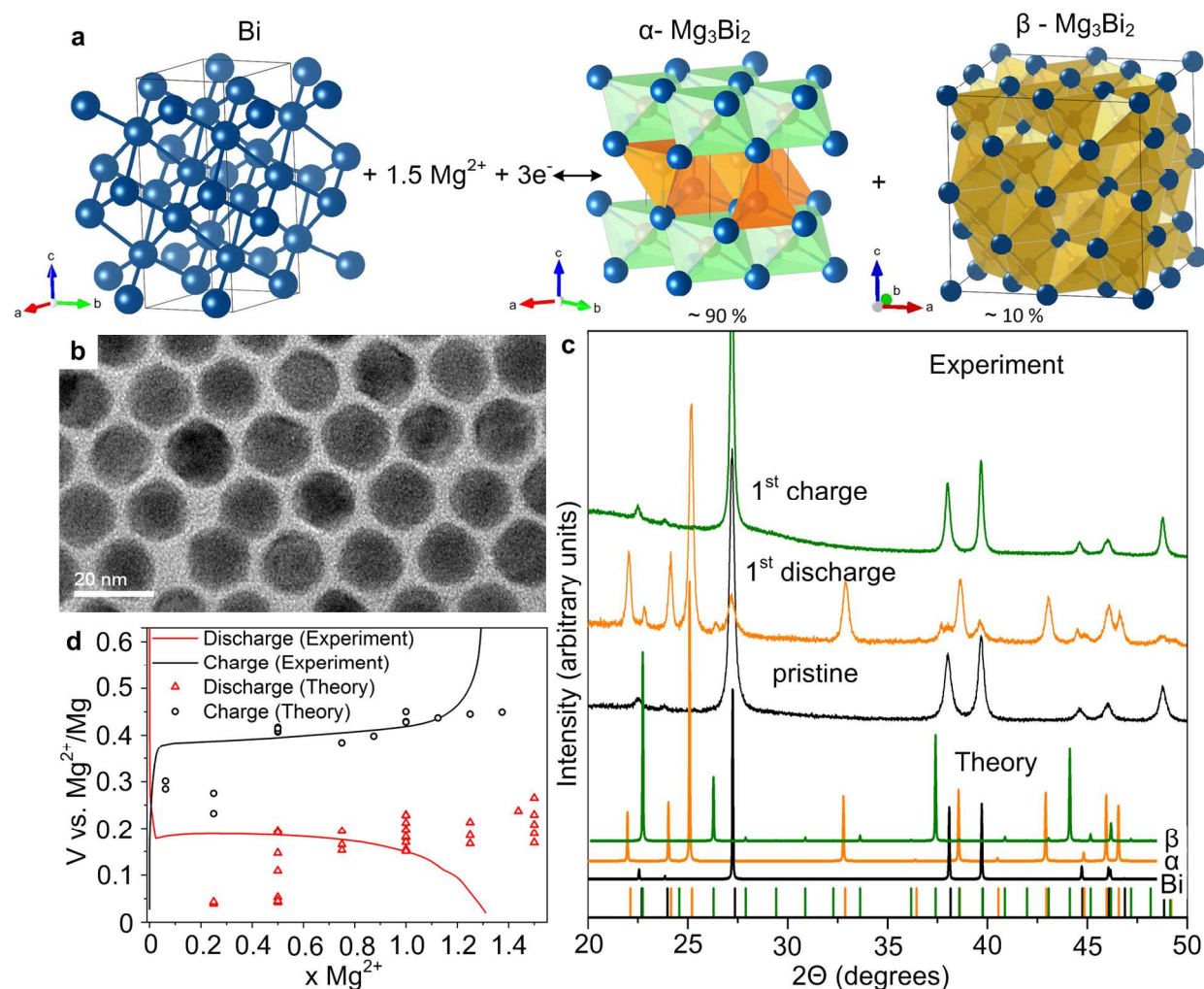
Figure 1. (a) The electrochemical magnesiation reaction of bismuth and the crystal structures of the relevant phases: elemental Bi (hexagonal), α-Mg_3Bi_2 (trigonal), and β-Mg_3Bi_2 (cubic(simulated)). The polyhedra show the tetrahedral (yellow) and octahedral (green) coordination environments of Mg by Bi atoms. (b) Transmission electron micrograph (TEM) of 18 nm Bi NCs prior to electrode fabrication. (c) Experimental powder X-ray diffraction (XRD) patterns of pristine (as-prepared) and discharged/charged Bi NC electrodes and simulated patterns of the three relevant Mg_xBi phases identified in (a). (d) Calculated and measured voltage profiles of the discharge/charge reactions for Bi NCs, expressed in volts per mole of Mg.

The enthalpies of formation of the α- and β-Mg_3Bi_2 phases are calculated to be -115.13 kJ mol^{-1} and -99.33 kJ mol^{-1}, respectively. The most important structural difference between these two polymorphs of Mg_3Bi_2 is the coordination environment(s) of the Mg atoms. In the α-phase trigonal structure, there are two non-equivalent Mg sites (Figure S1): one in the center of a

perfect, edge-sharing Bi octahedron (octahedral Mg, *1a* site) and one in the center of a distorted

(distortion index: 0.013 Å), edge-sharing Bi tetrahedron (tetrahedral Mg, *2d* site). In the β-phase

cubic structure, all of the Mg sites are symmetrically equivalent and occupy the centers of

distorted, edge-sharing Bi tetrahedra, which have a low distortion index of 0.009 Å.

Interestingly, the cubic β-Mg_3Bi_2 structure predicted herein differs from that reported by Barnes

et al.[104] Therein, only the neutron diffraction pattern lattice parameter was predicted, but the

exact crystallographic space group was not found. It was hypothesized that β-Mg_3Bi_2 has the

same space group as α-AgI and α-Ag_2Se, that is a body-centered cubic *Im-3m* structure (No

229).[104]

Electrochemical MIB cells were subsequently prepared and analyzed at various stages during

cycling to elucidate the magnesium insertion mechanism in Bi NCs. The magnesiation reaction

of Bi NCs was carried out in a half-cell configuration using Mg foil as the counter and reference

electrode and 0.2M/2M $Mg(BH4)_2$/$LiBH_4$ in diglyme as the electrolyte. The Coulombic

efficiency of Mg plaiting/stripping in $Mg(BH4)_2$/$LiBH_4$ was reported to be 100%.[53] The active

anode material comprised monodisperse 18 nm Bi NCs (Figure 1b and S3), synthesized using a

surfactant-assisted colloidal method as previously described.[105] Room temperature powder X-ray

diffraction (XRD) patterns of the Bi electrode were collected after electrochemical discharge

(Mg-insertion), confirming the formation of two phases as predicted in the simulations: the

trigonal and cubic Mg_3Bi_2 phases. The high-temperature cubic phase, β-Mg_3Bi_2, was the minor

component (~10% within 24 h after magnesiation was started, Figure 1c). The electrochemical

potential during magnesiation (*i.e.*, as a function of composition) calculated from the theoretical

enthalpy of reaction (Figure S4) correlates well with the measured voltage profiles of electrodes

prepared with 18 nm Bi NCs (Figure 1d, galvanostatic cycling using magnesium borohydride as

the electrolyte, see Methods for experimental details). Both galvanostatic discharge measurements and cyclic voltammetry (Figure S5) indicate that Mg-ion insertion occurs at 0.2 V followed by removal at 0.4 V. Flat magnesiation and de-magnesiation plateau regions suggest the absence of any intermediate crystalline phases.

The magnesiation reaction,

$$xMg + Bi \rightarrow Mg_xBi \qquad \text{(Equation 1)}$$

is calculated to be initially slightly endothermic, until x > 0.5 when the process becomes exothermic. Interestingly, between 0.5 < x < 1.25, variable composition states were found, indicating the possibility to vary the Mg content in that range of composition by only small changes of energy. No other local minima are found in the composition range between x = 0 and 1.5, in agreement with the experimental phase diagram.[103] Volume changes during the magnesiation reaction were also calculated since the structural stability of an electrode material is directly related to the volume change upon insertion/removal of ions. The insertion of Mg-ions into Bi is predicted to induce only a slight volume increase between 0 < x < 0.25; further insertion is accompanied by a linear dependence of the cell volume on the composition. When x = 1.5 (Mg_3Bi_2) is reached, the cell volume has more than doubled compared to the de-magnesiated state, enlarging from 30.98 $Å^3$ for elemental Bi to 138.13 $Å^3$ for α-Mg_3Bi_2 (Figure S6).

First-principles structure prediction is particularly valuable as a tool to gain insight into the coordination environment of each atomic species, and hence to determine the dominant factors (structural and energetic) that can impact the performance of a compound as an active electrode material. For example, vacancy formation energy and Mg atom conduction pathway isotropy/anisotropy are important properties to consider in the evaluation of electrode materials

for MIBs. In this work, preliminary results indicate that at a low concentration of Mg-vacancies, the enthalpies of vacancy formation in α-Mg$_3$Bi$_2$ are comparable on octahedral and tetrahedral sites (*e.g.*, +0.185 eV and +0.173 eV, respectively, at [V$_{Mg}$] = 0.125). At the same vacancy concentration, the enthalpy of Mg-vacancy formation in β-Mg$_3$Bi$_2$ is found to be significantly higher: +0.408 eV. In addition, the migration of Mg atoms is very different between the two phases of Mg$_3$Bi$_2$. In trigonal α-Mg$_3$Bi$_2$, Mg atom migration follows a tetrahedral-octahedral pathway, according to molecular dynamics simulations at 300 K. In the cubic β-Mg$_3$Bi$_2$, however, despite that the Mg sites are all symmetrically equivalent, the wider distribution of Mg-Mg distances causes the transport of Mg atoms to be anisotropic. The energetically favored route within β-Mg$_3$Bi$_2$ is the shortest Mg-Mg pathway which is found to be along the crystallographic **a**-direction, as shown in Figure S2.

Mesoscale Insights into the Electrochemistry of Nanocrystalline Bi Anodes. In addition to the inherent phase transitions that occur during charge/discharge cycling, it is often the case that morphological changes play a significant role in electrochemical performance of nanoscale electrode materials, especially for materials that undergo large volumetric changes. We investigate these effects herein by starting with uniform, spherical, highly-crystalline 18 nm Bi NCs and monitor the changes (both to the individual NCs themselves and the electrode as a whole) imparted as a result of electrode preparation and electrochemical cycling by performing *ex-situ* wide-angle XRD (Figure S7), TEM (Figure S8), and SAXS (Figure 2) measurements.

In order to prepare well-defined, model electrodes from uniform Bi NCs, several steps were undertaken prior to electrcochemical cycling. First, the highly insulating capping ligands left over from the NC synthesis were removed *via* a soft treatment method using hydrazine in acetonitrile (ACN), a common ligand-stripping procedure.[106-108] Subsequently, the bare Bi NCs

were ball-mixed with polyvinylidene fluoride (PVDF) as a binding material and carbon black (CB) as a conductive additive in n-methylpyrrolidone as a solvent, followed by casting and drying on copper foil as the current collector. The crystallite size of the monodisperse Bi NCs was found not to be affected by either the ligand removal procedure or the electrode fabrication, as determined by Scherrer analysis of the wide-angle XRD measurements (Figure S7, as-prepared electrodes are denoted as sample S1) and TEM studies (Figure S8). Just prior to assembling the electrochemical cells, the as-prepared Bi NC electrodes were further treated with hydrazine to remove traces of surface oxides (denoted as sample S2), which were found to inhibit Mg-ion insertion (presumably by the formation of electronically and ionically insulating MgO). This treatment was found to cause a doubling of the mean NC size (by XRD and TEM analysis), which may be attributed to the fusing of neighboring NCs once the surface oxides are removed. Subsequent electrochemical cycling (up to 100 cycles) did not cause a further increase in average NC size (Figures S7-S8), suggesting that after the initial hydrazine-induced fusion, the larger NCs become sufficiently well-separated.
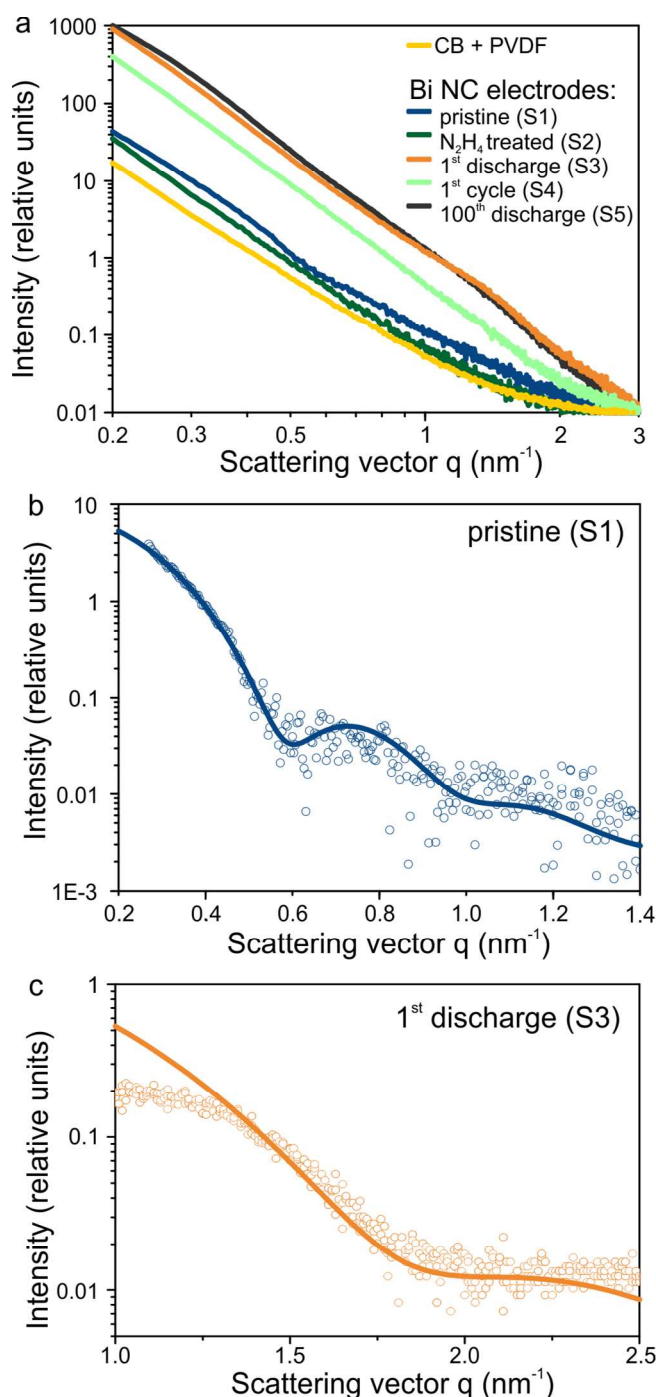
Figure 2. SAXS patterns of 18 nm Bi NC-based materials on Cu-foil. The scattered intensity is plotted as a function of the reciprocal scattering vector, q. (a) Log-log plots of all SAXS patterns collected: carbon black with binder (CB + PVDF, yellow) as a control and Bi NCs combined with CB and PVDF ("pristine electrode", blue), after hydrazine (N_2H_4) treatment (green), after the 1st discharge (orange), after the 1st complete cycle (light green), and after the 100th discharge (gray). (b) Log-normal plot of the pristine Bi NC electrode SAXS pattern after subtracting the CB + PVDF background. The measured data (circles) are fitted with a polydisperse sphere model (line) indicating an average diameter of 14.8 ± 0.5 nm. (c) Log-normal plot of the Bi NC

electrode SAXS pattern after hydrazine treatment and the 1st discharge, and after subtracting the CB + PVDF background. The experimental data (circles) are fitted with a polydisperse sphere model (line) indicating an average particle size of 4.4 ± 0.8 nm.

The mesoscale structure and morphology of complex materials can be sensitively probed using SAXS techniques, with applications ranging from the determination of the size and shape of crystalline and amorphous NPs to the symmetry and pore-to-pore spacing of ordered mesoporous materials, or even to investigations of the structure of electrolyte ions in microporous electrodes.[109] In this work, SAXS measurements of 18 nm Bi NC electrodes were performed at various stages of preparation and electrochemical cycling (Figure 2) to determine the average grain size and size distribution of the constituent particles within the overall electrode. The accessible length scale of these experiments was between 1-16 nm, corresponding to scattering vectors, q, between 3.0-0.2 nm^{-1}. A carbon black anode combined with binder (CB + PVDF, Figure 2a), investigated as a control sample, was found to exhibit the lowest integral scattering intensity, showing a linear dependence on q between 0.2-1 nm^{-1} with a Porod slope of -3.7. This pattern is typical of mesostructured materials with fractal surfaces such as carbon black.[110] Upon the fabrication of a pristine Bi NC electrode (sample S1), *i.e.,* when Bi NCs are added to the CB + PVDF mixture, the SAXS pattern exhibits the same background slope at 2.4 times higher integral scattering intensity. This higher intensity can be explained by the large scattering cross-section of Bi compared to carbon. The pristine sample also shows a local minimum at 0.6 nm^{-1} that can be caused by the scattering contribution of the shape function of the Bi NCs to the total scattering signal. After subtraction of the CB + PVDF background (Figure 2b), the scattering profile for separated nanometer-sized particles is more apparent. A polydisperse sphere model can be used to fit the experimental SAXS data, indicating a mean particle diameter of 14.8 ± 0.5 nm with a size distribution of 14% (averaged 10 times), generally in good agreement with TEM images and wide-angle XRD patterns (Figures S3, S7, and S8). Moreover, the factor of 2.4

increase in integral scattering intensity due to the addition of Bi to the CB + PVDF control electrode is consistent with calculations based on the comparison of a two-phase (carbon + vacuum) and three-phase (carbon + Bi + vacuum) polydisperse sphere model, using the known relative masses of Bi and carbon, the known electron densities of Bi and graphite, and a density of carbon black of 0.4 g cm^{-3}. The subsequent treatment of the pristine electrode with hydrazine to remove trace oxides (sample S2) causes the minimum at ~0.6 nm^{-1} to be less pronounced, which is consistent with the NC size enlargement measured by wide-angle XRD.

After the first electrochemical discharge, *i.e.*, magnesiation, of the hydrazine-treated electrode (sample S3), the SAXS intensity was found to be 16 times higher than that of the pre-cycled, hydrazine-treated electrode (sample S2) and the SAXS pattern was found to exhibit a broad minimum at ~1.9 nm^{-1}. Furthermore, upon the first charge, *i.e.*, de-magnesiation, of the discharged electrode (sample S4), the intensity was found to be reduced by a factor of 2, remaining 8 times higher than that of the pristine electrode (sample S1). The SAXS pattern of the same electrode after 100 discharges (sample S5) remains nearly identical to that of the sample after the first discharge, consistent with the high cycling stability of the electrodes as evidenced during electrochemical testing and discussed in the next section. The Porod slope of the SAXS pattern of the electrode after the first charge (sample S4) is -4.0, corresponding to a smoother surface of scattering particles.[111] This reduction in the slope (from -3.7 for the electrode before cycling) and thus smoothening of the CB surface can be explained by the filling of the mesopores (2-50 nm) of the CB particles by electrolyte. In a simplified description, this mesopore filling corresponds to an increased volume of the CB particles and a slightly increased average electron density of the CB particles compared to particles without such incorporated ions. Both effects would also lead to an increased integral scattering intensity, as was observed.

The higher intensity of the SAXS patterns of the discharged electrodes (samples S3 and S5) compared to that of the charged electrode (sample S4) indicates the successful incorporation of Mg-ions into the Bi NCs. This increase is quantitatively validated by taking into account the volumetric expansion by a factor of 2 and decrease in electron density of Mg_3Bi_2 compared to Bi.

The most prominent feature of the SAXS pattern after the first discharge (and likewise for all subsequent post-discharge patterns) is the broad hump centered at q = 1.9 nm^{-1} (Figures 2a and 2c) corresponding to nanostructures with a length or regularity of 4.5 nm as fitted to a polydisperse sphere model (Figure 1c). The SAXS intensity below 1.4 nm^{-1} could not accurately be fitted by this method, which can be explained either by the agglomeration of ~4.5 nm NPs, by the formation of ~4.5 nm grains within larger Mg_3Bi_2 aggregates, or by a mixture of larger and smaller particles. The faint intensity modulation of the SAXS pattern of Bi NCs after 100 cycles (S5 in Figure 2a) indicates the existence of larger particles after cycling. The modulation between 0.2 and 0.7 nm^{-1} is attributed to structures in the size range between 20 to 40 nm, which is consistent with the crystallite sizes derived from XRD analysis as shown in Figure S7. The wide-angle XRD peaks, however, do not show any pronounced broadening between the 1st charge and the 100th charge; instead, a moderate decrease in crystallite size from 35 to 25 nm is observed, accompanied by a pronounced decrease in peak intensity. This transition is reflected in the smooth and featureless SAXS pattern after the 1st discharge (S4 in Figure 2a) corresponding to scattering from large uniform particles compared to the more modulated pattern after the 100th discharge (S5 in Figure 2a) comprising an additional hump at higher q related to the formation of smaller particles. The lack of broadening in the wide-angle XRD peaks indicates that these

newly formed, smaller particles are amorphous in nature, in accordance with the decrease in the Bragg peak intensities.

The results from this *ex-situ* SAXS study of Bi NC anodes at various stages during electrode preparation and electrochemical cycling can be used to correlate structural changes in the electrode to the electrochemical behavior of the full-cell device. Firstly, it is clear that the amorphization and reduction in size from 15 to 5 nm of a considerable fraction of the active Bi particles already occurs after the first discharge process, and is therefore directly related to the incorporation of Mg into the NCs. In other words, this effect can be seen as a result of the formation of the α-Mg_3Bi_2 and β-Mg_3Bi_2 phases. The corresponding peak in the SAXS pattern then remains constant over the next 100 charge/discharge cycles and shows only a slight shift to lower q indicating a slight further increase in the active Bi particle diameter (S3 and S5 in Figure 2a).[109] A schematic depiction of the size evolution of 18 nm Bi NCs upon electrode preparation, hydrazine treatment, and electrochemical cycling is given in Figure S9.

Half-Cell Electrochemical Performance: Capacity, Rate Capability and Cyclability. The charge and discharge capacities of Bi NC electrodes (prepared with CB + PVDF, and treated with hydrazine to remove surface oxides) at a rate of 0.5C were found to be 331 and 335 mAh g^{-1} (corresponding to x = 1.3 in Figure 1d), respectively, which corresponds to ~90% of the theoretical capacity (x = 1.5). The effect of crystallite size on the rate performance of Bi anodes was investigated by preparing electrodes from spherical Bi NCs (both 10 and 18 nm) and milled microcrystalline Bi (0.5-2 µm crystallites, "bulk"), the details of which are shown in Figure S3. Surprisingly, relatively high capacities were measured for all cells even under discharge rates of up to 20C (*i.e.*, fully discharged in 3 minutes) with a high coulombic efficiency of > 98%. The lowest capacities measured were for bulk Bi at high current rates (Figure 3a). No advantages

were observed to be gained by reducing the size of Bi NCs from 18 to 10 nm, with

systematically poorer capacities measured at all rates. Cells incorporating Bi NCs showed a high

capacity retention of 93% after 150 cycles at a rate of 2C (for both 10 and 18 nm NCs).

Electrodes containing 18 nm Bi NCs also exhibited a noteworthy capacity retention of 54% after

4500 cycles at 20C (Figure S10). On the other hand, the capacity of electrodes prepared with

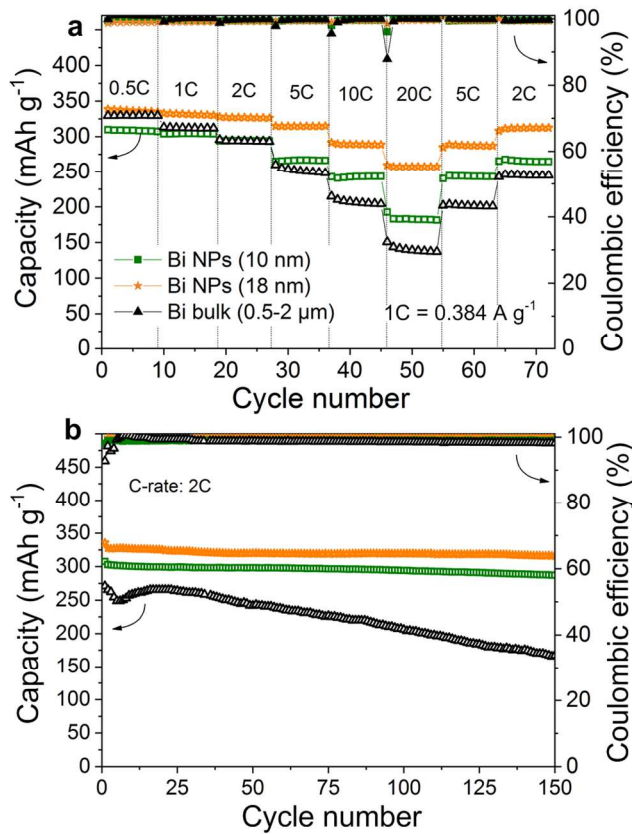bulk Bi were found to significantly decrease upon electrochemical cycling (Figure 3b).

Figure 3. (a) Rate capability measurements of Mg-ion half-cells incorporating Bi anodes derived from monodisperse Bi NCs (10 and 18 nm) or microcrystalline Bi (0.5-2 μm, "bulk"). (b) Cycling stability of the same Bi anodes at a current density of 2C (0.77 A g^{-1}). All electrodes were prepared with the same composition of Bi(64%)/CB(21%)/PVDF(15%), by weight, and a 0.2M/2M solution of magnesium borohydride/lithium borohydride in diglyme was used as the electrolyte.

Full-Cell Electrochemical Experiments Utilizing Bi Nanocrystal Anodes. The key potential

benefit of Bi (and similar alloying materials) as a model anode for MIBs arises from its

compatibility with more desirable electrolytes within which metallic Mg does not reversibly electroplate. To demonstrate this utility, full-cell electrochemical experiments were conducted using Mo_6S_8 (Chevrel phase) as a standard cathode.[45] Anode-limited cells were assembled using anodes prepared from 18 nm Bi NCs, as previously described. As a representative electrolyte (in which metallic Mg does not operate reversibly), a 1M solution of $Mg(TFSI)_2$ in diglyme was used. Compared to borohydride-based electrolytes, $Mg(TFSI)_2$ in diglyme is much safer and constitutes only earth-abundant elements, and is therefore a desirable alternative. Hence, a more common $Mg(BH_4)_2/LiBH_4$ electrolyte was also tested for comparison. In both cases, Mo_6S_8 cathodes were first pre-charged (magnesiated) using half-cells with metallic Mg as the anode and $Mg(BH_4)_2/LiBH_4$ as the electrolyte. With both $Mg(TFSI)_2$ and borohydride electrolytes, Bi NC anodes were found to exhibit similar capacities and fully reversible operation (Figure 4, Figure S11). Importantly, higher voltages (corresponding to higher energy storage densities) and more desirable voltage profiles were obtained with $Mg(TFSI)_2$ as the electrolyte.
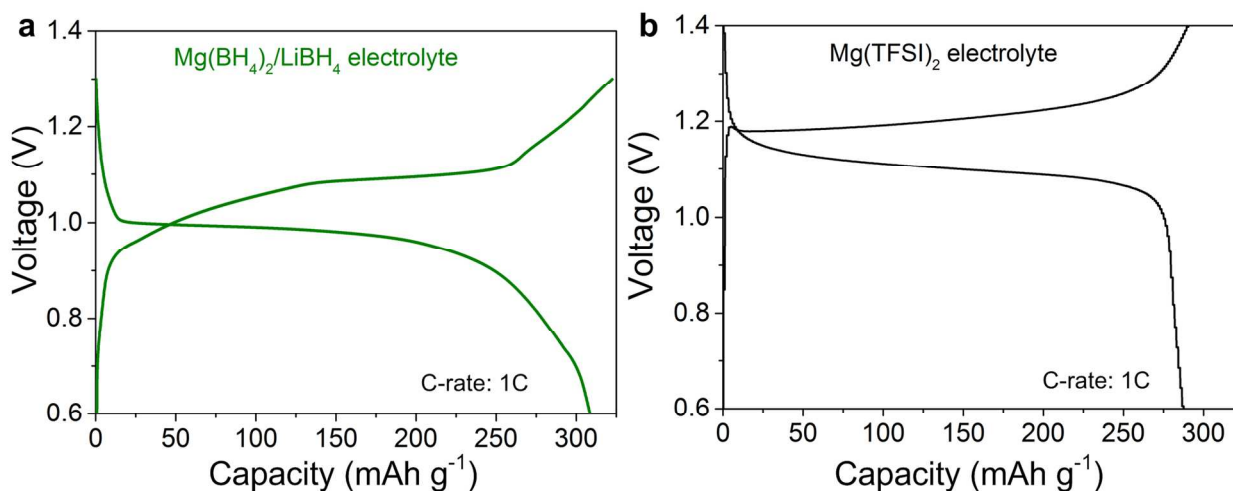

Figure 4. Typical discharge/charge voltage profiles of anode-limited full-cell MIBs (Bi–Mo_6S_8) at a rate of 1C (0.384 A g^{-1}) with (a) $Mg(BH_4)_2/LiBH_4$ and (b) $Mg(TFSI)_2$ as the electrolyte. The full-cell capacities are normalized to the mass of Bi.

CONCLUSIONS

In this work, colloidal Bi NCs were demonstrated as a well-defined model system for understanding the effects of structural changes, crystallinity, and morphology on electrochemical properties of Bi anodes for Mg-ion batteries upon discharge/charge (magnesiation/demagnesiation) cycling. Furthermore, Bi anodes can operate with a broader range of Mg-ion electrolytes, in particular with those made of oxidatively stable salts and solvents, offering important opportunities for the exploration of cathode materials operating above 3 V *vs.* Mg^{2+}/Mg. While metallic Mg remains the eventual ideal anode material for MIBs, the short term benefits of exploring a wide range of electrolyte and cathode combinations together with Bi as the anode could greatly accelerate research in the direction of high energy density, abundant element-based secondary batteries.

Specifically, it has been revealed that the intercalation of Mg within Bi NCs takes place through an alloying mechanism, leading to the simultaneous formation of α-Mg_3Bi_2 and β-Mg_3Bi_2 as confirmed by XRD measurements. First-principles crystal structure prediction methodologies enabled the identification and characterization of the β-phase of Mg_3Bi_2 (cubic, *Ia-3* space group). The first electrochemical discharge of the as-prepared Bi NC electrode (after hydrazine treatment, which initially causes particle fusing) disturbs the monodisperse and crystalline nature of the active particles, leading to the formation of smaller nanostructures and amorphous particles. However, over the subsequent 100 discharge/charge cycles, the electrode structure and electrochemical performance remain nearly unchanged. Bi NC anodes were also found to exhibit a high retention of capacity upon extended cycling, losing only 7% of their initial capacity over 150 cycles at a rate of 2C (770 mA g^{-1}).

METHODS

Chemicals. Bismuth (III) chloride (99,999%, Sigma-Aldrich), 2.7 M n-butyllithium solution in heptane (Bu-Li, Aldrich), Oleylamine (OLA, Acros), Oleic acid (OA, 90%, Aldrich), Toluene (99.9%, Sigma-Aldrich), Ethanol (Fluka), Hydrazine (Gerling Holz+Co), Acetonitrile (ACN, max. 0.005% H_2O, Merck), Potassium chloride (KCl, Fluka), Molybdenum (IV) sulfide (MoS_2, 99%, Aldrich), Cupper sulfide (CuS, 99.5%, STREM), Molybdenum (Mo, 99.7%, Fluka).

Battery components. Bismuth (325 mesh, 99.5%, Alfa-Aesar), carbon black (CB, Super C65, provided by TIMCAL), Mg electrolyte (0.2M and 2M solution of magnesium borohydride ($Mg(BH_4)_2$, 95%, Sigma Aldrich) and lithium borohydride ($LiBH_4$, >95%, Sigma Aldrich) in diethylene glycol dimethyl ether (diglyme, anhydrous, 99.5%, Sigma Aldrich)), conventional Mg electrolyte (0.25M solution of Bis(trifluoromethanesulfonyl)imide, ($Mg(TFSI)_2$, 99.5%, in diglyme, Solvionic SA), glass-fiber separator (EUJ-grade, Hollingsworth & Vose Company Ltd., United Kingdom), poly(vinylidene flouride) (PVDF, average MW ~ 534 g mol^{-1}, Sigma Aldrich), and N-Methyl-2-pyrrolidone (NMP, 99%, Sigma Aldrich).

Synthesis of Bi NCs. In a typical synthesis of ~18 nm Bi NCs,[105] 12 mL of dried OLA and 0.2 mmol of $BiCl_3$ (0.063 g) were added into a 50 mL three-neck flask and dried under vacuum for 20 minutes at 60℃ while stirring. In parallel, 3.6 mmol of Bu-Li (1.33 mL) was prepared in an inert atmosphere glovebox. The temperature of the OLA/$BiCl_3$ solution was then increased to 130 °C under nitrogen, and the Bu-Li solution was injected. The solution color turned dark brown immediately, indicating the formation of Bi NCs. After 300 seconds, the reaction was quickly ended by the injecting 12 mL of anhydrous toluene and cooled down to room temperature in ice-water bath. Then, 0.2 mL of OA was added at 50 °C. Bi NCs were precipitated by 25 mL of ethanol following centrifugation at 7000 rpm for 4 min. Then Bi NCs were redispersed in 5

mL of toluene containing 100 µL of OA to replace the weakly bound OLA, and then precipitated

by 5 mL of ethanol, followed by centrifugation at 7000 rpm for 2 min. Finally, the Bi NCs were

redispersed in toluene. The synthesis of 10 nm Bi NCs has been conducted analogously to 18 nm

Bi NCs, except for the Bu-Li injection temperature (70°C) and reaction time (10 sec).

Ligand-removal of Bi NCs. In order to remove the organic capping ligands, NCs were

precipitated with EtOH, centrifuged and suspended in a solution of 0.8 mL hydrazine in 25 mL

anhydrous acetonitrile. The suspension was stirred at room temperature for two hours. After

centrifugation (8000 rpm, 4 min), the precipitate was washed three times with acetonitrile (~ 20

mL) to remove residual hydrazine. Finally, NCs were separated from the solution by

centrifugation (8000 rpm, 4 min) and dried for 12 h at room temperature under vacuum.

Electrochemical cell preparation and testing. Bi electrodes were prepared by ball-milling of

the respective Bi NCs after ligand removal or bulk Bi (64 wt.%) with carbon black (21 wt.%)

and PVDF binder (15 wt.%) in NMP solvent for 1 h and casting the obtained slurry onto Cu foil.

The onset of electrochemical oxidation for the Cu current collector occurs at 1.5 V vs. Mg^{2+}/Mg

in $Mg(BH_4)_2$/$LiBH_4$ electrolyte (Figure S12). Mo_6S_8 electrodes were prepared in the same way

using Mo_6S_8 powder (80 wt.%), carbon black (10 wt.%) and PVDF binder (10 wt%). Mo_6S_8 was

synthesized by the molten salt synthesis, as described elsewhere.[112] The current collectors were

then dried for 12 h at 80 °C in a vacuum oven. Additionally, shortly before assembling the

batteries, the Bi electrodes were immersed in hydrazine solution in ACN (C = 25 vol.%) for 6 h

following drying at 75 °C for 6 h. In the case of bulk Bi electrodes, pure hydrazine was used

instead of its solution. **Caution:** hydrazine is an extremely toxic and dangerously unstable liquid.

Hydrazine treatment should be carried out only by appropriately trained personnel under air-free

conditions (*e.g.*, in a glovebox).

Coin-type cells were assembled in a glovebox using a one layer glass fiber separator. Polished Mg metal served as both reference and counter electrode. Two electrolytes tested were 0.2M and 2M solution of, correspondingly, magnesium borohydride and lithium borohydride in diethylene glycol dimethyl ether and 0.25M solution of $Mg(TFSI)_2$ in diglyme were used. Half and full cells were cycled between 0.02 – 0.63 V and 0.220 – 1.35 V, respectively, on an MPG2 multi-channel workstation (Bio-Logic). The obtained capacities for half and full cells were normalized to the mass of Bi. Prior to electrochemical cycling, Bi electrodes were cycled for 10 cycles between 0.02 – 0.63 V using cyclic voltammetry at a scan rate of 0.1 mV s^{-1}. As consistent with electrochemical impedance analysis (Figure S13), the impedance of the cell decreases considerably during the initial 10 cycles.

Materials Characterization. TEM was performed using a Philips CM30 microscope operated at 300 kV. High-resolution TEM (HRTEM) was performed using a JEOL 2200FS microscope at 200 kV. Samples were mounted on carbon-coated TEM grids (Ted-Pella). Wide-angle powder XRD measurements were performed using a STOE STADI P diffractometer. SAXS measurements were performed using a Bruker Nanostar on samples held under vacuum.

DFT and molecular dynamics simulations. The starting host lattice for the Mg-Bi system was the rhombohedral structure of elemental bismuth. By combining the cluster expansion approach, interfaced with Quantum ESPRESSO DFT-based total energy calculations, and Ab-initio Random Structure Searching (AIRSS) coupled with CASTEP calculations, we mapped the potential energy surface (PES) in the full composition range of of Mg-Bi system. The geometry optimizations of the final stable structures reported in the present work were obtained by using CASTEP calculations. We used norm-conserving pseudopotentials and reciprocal space representation of Mg and Bi atoms, whose valence shells contain respectively 10 electrons,

$2s^2 2p^6 3s^2$ states, and 15 electrons, $5d^{10} 6s^2 6p^3$ states. The different exchange-correlation functionals were checked in the lattice optimization, in order to reproduce the lattice parameters as much as closer to the reported ones for the elemental phases, Mg and Bi and the binary phase, Mg_3Bi_2, which represent the initial state and the final state of the Mg-Bi phase space considered in the present work. While the geometry optimization of the elemental phases, Mg and Bi, reproduced better the respective lattice parameters by using the non-local potential GGA-PBE, the local potential LDA-CA-PZ[113-114] reproduced lattice parameters of Mg_3Bi_2 closer to the experimentally reported ones. Based on that, in the final step of structure optimization of the binary phases, we used LDA potential with a cut-off energy of 720 eV and a k-point mesh density of at least 0.02 Å^{-1}. To investigate the motion of Mg atoms in the charge reaction we performed preliminary molecular dynamics calculations with NVT ensemble and by using a supercell comprising 2x2x2 unit cells and k-point sampling at gamma point. The temperature was set to 27 °C by using Hoover-Langevin thermostat and 1fs for the time step. The total simulation time was 10 ps.

ASSOCIATED CONTENT

Supporting Information. Supporting Figures S1-S8 and Table S1. This material is available free of charge *via* the Internet at http://pubs.acs.org.

AUTHOR INFORMATION

Corresponding Author

*mvkovalenko@ethz.ch (M.V.K.)

REFERENCES

1. Ulvestad, A.; Singer, A.; Clark, J. N.; Cho, H. M.; Kim, J. W.; Harder, R.; Maser, J.; Meng, Y. S.; Shpyrko, O. G., Topological Defect Dynamics in Operando Battery Nanoparticles. *Science* **2015,** *348*, 1344-1347.
2. Xu, L.; Kim, C.; Shukla, A. K.; Dong, A.; Mattox, T. M.; Milliron, D. J.; Cabana, J., Monodisperse Sn Nanocrystals as a Platform for the Study of Mechanical Damage during Electrochemical Reactions with Li. *Nano Lett.* **2013,** *13*, 1800−1805.
3. Oszajca, M. F.; Bodnarchuk, M. I.; Kovalenko, M. V., Precisely Engineered Colloidal Nanoparticles and Nanocrystals for Li-Ion and Na-Ion Batteries: Model Systems or Practical Solutions? *Chem. Mater.* **2014,** *26*, 5422-5432.

4.   Oh, M. H.; Yu, T.; Yu, S.-H.; Lim, B.; Ko, K.-T.; Willinger, M.-G.; Seo, D.-H.; Kim, B. H.; Cho, M. G.; Park, J.-H.; Kang, K.; Sung, Y.-E.; Pinna, N.; Hyeon, T., Galvanic Replacement Reactions in Metal Oxide Nanocrystals. *Science* **2013,** *340*, 964-968.

5.   Liu, X. H.; Zhong, L.; Huang, S.; Mao, S. X.; Zhu, T.; Huang, J. Y., Size-Dependent Fracture of Silicon Nanoparticles During Lithiation. *ACS Nano* **2012,** *6*, 1522–1531.

6.   Aifantis, K. E.; Haycock, M.; Sanders, P.; Hackney, S. A., Fracture of Nanostructured Sn/C Anodes During Li-insertion. *Mater. Sci. Eng. A* **2011,** *529*, 55-61.

7.   Koo, B.; Xiong, H.; Slater, M. D.; Prakapenka, V. B.; Balasubramanian, M.; Podsiadlo, P.; Johnson, C. S.; Rajh, T.; Shevchenko, E. V., Hollow Iron Oxide Nanoparticles for Application in Lithium Ion Batteries. *Nano Lett.* **2012,** *12*, 2429−2435.

8.   Wang, S.; He, M.; Walter, M.; Krumeich, F.; Kravchyk, K. V.; Kovalenko, M. V., Monodisperse $CoSn_2$ and $FeSn_2$ Nanocrystals as High-Performance Anode Materials for Lithium-Ion Batteries. *Nanoscale* **2018,** *10*, 6827-6831.

9.   Chan, C. K.; Peng, H.; Liu, G.; McIlwrath, K.; Zhang, X. F.; Huggins, R. A.; Cui, Y., High-Performance Lithium Battery Anodes Using Silicon Nanowires. *Nat. Nanotechnol.* **2008,** *3*, 31-35.

10.   Magasinski, A.; Dixon, P.; Hertzberg, B.; Kvit, A.; Ayala, J.; Yushin, G., High-Performance Lithium-Ion Anodes Using a Hierarchical Bottom-Up Approach. *Nat. Mater.* **2010,** *9*, 353-358.

11.   Kovalenko, I.; Zdyrko, B.; Magasinski, A.; Hertzberg, B.; Milicev, Z.; Burtovyy, R.; Luzinov, I.; Yushin, G., A Major Constituent of Brown Algae for Use in High-Capacity Li-Ion Batteries. *Science* **2011,** *334*, 75-79.

12.   Chockla, A. M.; Klavetter, K. C.; Mullins, C. B.; Korgel, B. A., Tin-Seeded Silicon Nanowires for High Capacity Li-Ion Batteries. *Chem. Mater.* **2012,** *24*, 3738-3745.

13.   Kravchyk, K. V.; Zünd, T.; Wörle, M.; Kovalenko, M. V.; Bodnarchuk, M. I., $NaFeF_3$ Nanoplates as Low-Cost Sodium and Lithium Cathode Materials for Stationary Energy Storage. *Chem. Mater.* **2018,** *30*, 1825-1829.

14.   Guntlin, C. P.; Zund, T.; Kravchyk, K. V.; Worle, M.; Bodnarchuk, M. I.; Kovalenko, M. V., Nanocrystalline FeF_3 and MF_2 (M = Fe, Co, and Mn) from Metal Trifluoroacetates and Their Li(Na)-Ion Storage Properties. *J. Mater. Chem. A* **2017,** *5*, 7383-7393.

15.   Oszajca, M. F.; Kravchyk, K. V.; Walter, M.; Krieg, F.; Bodnarchuk, M. I.; Kovalenko, M. V., Colloidal BiF_3 Nanocrystals: a Bottom-Up Approach to Conversion-Type Li-Ion Cathodes. *Nanoscale* **2015,** *7*, 16601-16605.

16.   Kim, C.; Adil, A. A.; Bayliss, R. D.; Kinnibrugh, T. L.; Lapidus, S. H.; Nolis, G. M.; Freeland, J. W.; Phillips, P. J.; Yi, T.; Yoo, H. D.; Kwon, B. J.; Yu, Y.-S.; Klie, R.; Chupas, P. J.; Chapman, K. W.; Cabana, J., Multivalent Electrochemistry of Spinel $Mg_xMn_{3-x}O_4$ Nanocrystals. *Chem. Mater.* **2018,** *30*, 1496-1504.

17.   Yaghoobnejad Asl, H.; Fu, J.; Kumar, H.; Welborn, S. S.; Shenoy, V. B.; Detsi, E., *In Situ* Dealloying of Bulk Mg_2Sn in Mg-Ion Half Cell as an Effective Route to Nanostructured Sn for High Performance Mg-Ion Battery Anodes. *Chem. Mater.* **2018,** *30*, 1815-1824.

18.   Hayner, C. M.; Zhao, X.; Kung, H. H., Materials for Rechargeable Lithium-Ion Batteries. *Annu. Rev. Chem. Biomol. Eng.* **2012,** *3*, 445-471.

19.   Palomares, V.; Casas-Cabanas, M.; Castillo-Martínez, E.; Han, M. H.; Rojo, T., Update on Na-Based Battery Materials. A Growing Research Path. *Energy Environ. Sci.* **2013,** *6*, 2312-2337.

20.   Park, C.-M.; Kim, J.-H.; Kim, H.; Sohn, H.-J., Li-Alloy Based Anode Materials for Li Secondary Batteries. *Chem. Soc. Rev.* **2010,** *39*, 3115-3141.

21.   Kim, Y.; Park, Y.; Choi, A.; Choi, N. S.; Kim, J.; Lee, J.; Ryu, J. H.; Oh, S. M.; Lee, K. T., An Amorphous Red Phosphorus/Carbon Composite as a Promising Anode Material for Sodium Ion Batteries. *Adv. Mater.* **2013,** *25*, 3045-3049.

22.   Goriparti, S.; Miele, E.; De Angelis, F.; Di Fabrizio, E.; Proietti Zaccaria, R.; Capiglia, C., Review on Recent Progress of Nanostructured Anode Materials for Li-Ion Batteries. *J. Power Sources* **2014,** *257*, 421-443.

23.   Nitta, N.; Wu, F.; Lee, J. T.; Yushin, G., Li-Ion Battery Materials: Present and Future. *Mater.Today* **2015,** *18*, 252-264.

24.   Dahbi, M.; Yabuuchi, N.; Kubota, K.; Tokiwa, K.; Komaba, S., Negative Electrodes for Na-Ion Batteries. *Phys. Chem. Chem. Phys.* **2014,** *16*, 15007-15028.

25.   Kim, S.-W.; Seo, D.-H.; Ma, X.; Ceder, G.; Kang, K., Electrode Materials for Rechargeable Sodium-Ion Batteries: Potential Alternatives to Current Lithium-Ion Batteries. *Adv. Energy Mater.* **2012,** *2*, 710-721.

26.   Palomares, V.; Serras, P.; Villaluenga, I.; Hueso, K. B.; Carretero-Gonzalez, J.; Rojo, T., Na-Ion Batteries, Recent Advances and Present Challenges to Become Low Cost Energy Storage Systems. *Energy Environ. Sci.* **2012,** *5*, 5884-5901.

27.   Obrovac, M. N.; Chevrier, V. L., Alloy Negative Electrodes for Li-Ion Batteries. *Chem. Rev.* **2014,** *114*, 11444-11502.

28.   Kim, Y.; Ha, K.-H.; Oh, S. M.; Lee, K. T., High-Capacity Anode Materials for Sodium-Ion Batteries. *Chem. Eur. J.* **2014,** *20*, 11980-11992.

29.   Su, X.; Wu, Q.; Li, J.; Xiao, X.; Lott, A.; Lu, W.; Sheldon, B. W.; Wu, J., Silicon-Based Nanomaterials for Lithium-Ion Batteries: A Review. *Adv. Energy Mater.* **2014,** *4*, 1300882.

30.   Kundu, D.; Talaie, E.; Duffort, V.; Nazar, L. F., The Emerging Chemistry of Sodium Ion Batteries for Electrochemical Energy Storage. *Angew. Chem. Int. Ed.* **2015,** *54*, 3431-3448.

31.   Walter, M.; Erni, R.; Kovalenko, M. V., Inexpensive Antimony Nanocrystals and Their Composites with Red Phosphorus as High-Performance Anode Materials for Na-Ion Batteries. *Sci. Rep.* **2015,** *5*, 08418.

32.   Walter, M.; Bodnarchuk, M. I.; Kravchyk, K. V.; Kovalenko, M. V., Evaluation of Metal Phosphide Nanocrystals as Anode Materials for Na-Ion Batteries. *Chimia* **2015,** *69*, 724-728.

33.   Caputo, R., An Insight into Sodiation of Antimony from First-Principles Crystal Structure Prediction. *J. Electron. Mater.* **2016,** *45*, 999-1010.

34.   Liu, J.; Wang, S.; Kravchyk, K.; Ibáñez, M.; Krumeich, F.; Widmer, R.; Nasiou, D.; Meyns, M.; Llorca, J.; Arbiol, J.; Kovalenko, M. V.; Cabot, A., SnP Nanocrystals as Anode Materials for Na-Ion Batteries. *J. Mater. Chem. A* **2018,** *6*, 10958-10966.

35.   He, M.; Kravchyk, K.; Walter, M.; Kovalenko, M. V., Monodisperse Antimony Nanocrystals for High-Rate Li-Ion and Na-Ion Battery Anodes: Nano *versus* Bulk. *Nano Lett.* **2014,** *14*, 1255-1262.

36.   Kravchyk, K.; Protesescu, L.; Bodnarchuk, M. I.; Krumeich, F.; Yarema, M.; Walter, M.; Guntlin, C.; Kovalenko, M. V., Monodisperse and Inorganically Capped Sn and Sn/SnO_2 Nanocrystals for High-Performance Li-Ion Battery Anodes. *J. Am. Chem. Soc.* **2013,** *135*, 4199-4202.

37.   He, M.; Walter, M.; Kravchyk, K. V.; Erni, R.; Widmer, R.; Kovalenko, M. V., Monodisperse SnSb Nanocrystals for Li-Ion and Na-Ion Battery Anodes: Synergy and Dissonance Between Sn and Sb. *Nanoscale* **2015,** *7*, 455-459.

38.   Tarascon, J. M.; Armand, M., Issues and Challenges Facing Rechargeable Lithium Batteries. *Nature* **2001,** *414*, 359-367.

39.   Li, Z.; Huang, J.; Yann Liaw, B.; Metzler, V.; Zhang, J., A Review of Lithium Deposition in Lithium-Ion and Lithium Metal Secondary Batteries. *J. Power Sources* **2014,** *254*, 168-182.

40.   Jäckle, M.; Groß, A., Microscopic Properties of Lithium, Sodium, and Magnesium Battery Anode Materials Related to Possible Dendrite Growth. *J. Chem. Phys.* **2014,** *141*, 174710.

41.   Wood, K. N.; Noked, M.; Dasgupta, N. P., Lithium Metal Anodes: Toward an Improved Understanding of Coupled Morphological, Electrochemical, and Mechanical Behavior. *ACS Energy Lett.* **2017,** *2*, 664-672.

42.   Yoo, H. D.; Shterenberg, I.; Gofer, Y.; Gershinsky, G.; Pour, N.; Aurbach, D., Mg Rechargeable Batteries: An On-Going Challenge. *Energy Environ. Sci.* **2013,** *6*, 2265-2279.

43.   Muldoon, J.; Bucur, C. B.; Gregory, T., Quest for Nonaqueous Multivalent Secondary Batteries: Magnesium and Beyond. *Chem. Rev.* **2014,** *114*, 11683-11720.

44.   Park, M.-S.; Kim, J.-G.; Kim, Y.-J.; Choi, N.-S.; Kim, J.-S., Recent Advances in Rechargeable Magnesium Battery Technology: A Review of the Field's Current Status and Prospects. *Isr. J. Chem.* **2015,** *55*, 570-585.

45.   Aurbach, D.; Lu, Z.; Schechter, A.; Gofer, Y.; Gizbar, H.; Turgeman, R.; Cohen, Y.; Moshkovich, M.; Levi, E., Prototype Systems for Rechargeable Magnesium Batteries. *Nature* **2000,** *407*, 724-727.

46.   Shterenberg, I.; Salama, M.; Gofer, Y.; Levi, E.; Aurbach, D., The Challenge of Developing Rechargeable Magnesium Batteries. *MRS Bull.* **2014,** *39*, 453-460.

47.   Canepa, P.; Sai Gautam, G.; Hannah, D. C.; Malik, R.; Liu, M.; Gallagher, K. G.; Persson, K. A.; Ceder, G., Odyssey of Multivalent Cathode Materials: Open Questions and Future Challenges. *Chemical Reviews* **2017,** *117*, 4287-4341.

48.   Pan, H.; Hu, Y.-S.; Chen, L., Room-Temperature Stationary Sodium-Ion Batteries for Large-Scale Electric Energy Storage. *Energy Environ. Sci.* **2013,** *6*, 2338-2360.

49.   Emsley, J., *Nature's Building Blocks: An A-Z Guide to the Elements*. OUP Oxford: 2011; p 699-699.

50.   Mohtadi, R.; Mizuno, F., Magnesium Batteries: Current State of the Art, Issues and Future Perspectives. *Beilstein J. Nanotechnol.* **2014,** *5*, 1291-1311.

51.   Yagi, S.; Ichitsubo, T.; Shirai, Y.; Yanai, S.; Doi, T.; Murase, K.; Matsubara, E., A Concept of Dual-Salt Polyvalent-Metal Storage Battery. *J. Mater. Chem. A* **2014,** *2*, 1144-1149.

52.   Tutusaus, O.; Mohtadi, R., Paving the Way towards Highly Stable and Practical Electrolytes for Rechargeable Magnesium Batteries. *ChemElectroChem* **2015,** *2*, 51-57.

53.   Shao, Y.; Liu, T.; Li, G.; Gu, M.; Nie, Z.; Engelhard, M.; Xiao, J.; Lv, D.; Wang, C.; Zhang, J.-G.; Liu, J., Coordination Chemistry in Magnesium Battery Electrolytes: How Ligands Affect Their Performance. *Sci. Rep.* **2013,** *3*, 3130.

54.   Vardar, G.; Sleightholme, A. E. S.; Naruse, J.; Hiramatsu, H.; Siegel, D. J.; Monroe, C. W., Electrochemistry of Magnesium Electrolytes in Ionic Liquids for Secondary Batteries. *ACS Appl. Mater. Interfaces* **2014,** *6*, 18033-18039.

55.   Canepa, P.; Gautam, G. S.; Malik, R.; Jayaraman, S.; Rong, Z.; Zavadil, K. R.; Persson, K.; Ceder, G., Understanding the Initial Stages of Reversible Mg Deposition and Stripping in Inorganic Nonaqueous Electrolytes. *Chem. Mater.* **2015,** *27*, 3317-3325.

56.   Rajput, N. N.; Qu, X.; Sa, N.; Burrell, A. K.; Persson, K. A., The Coupling between Stability and Ion Pair Formation in Magnesium Electrolytes from First-Principles Quantum Mechanics and Classical Molecular Dynamics. *J. Am. Chem. Soc.* **2015,** *137*, 3411-3420.

57.   Yoo, H. D.; Liang, Y.; Dong, H.; Lin, J.; Wang, H.; Liu, Y.; Ma, L.; Wu, T.; Li, Y.; Ru, Q.; Jing, Y.; An, Q.; Zhou, W.; Guo, J.; Lu, J.; Pantelides, S. T.; Qian, X.; Yao, Y., Fast Kinetics of Magnesium Monochloride Cations in Interlayer-expanded Titanium Disulfide for Magnesium Rechargeable Batteries. *Nat. Commun.* **2017,** *8*, 339.

58.   Doe, R. E.; Han, R.; Hwang, J.; Gmitter, A. J.; Shterenberg, I.; Yoo, H. D.; Pour, N.; Aurbach, D., Novel, Electrolyte Solutions Comprising Fully Inorganic Salts with High Anodic Stability for Rechargeable Magnesium Batteries. *Chem. Commun.* **2014,** *50*, 243-245.

59.   Zhang, Z.; Cui, Z.; Qiao, L.; Guan, J.; Xu, H.; Wang, X.; Hu, P.; Du, H.; Li, S.; Zhou, X.; Dong, S.; Liu, Z.; Cui, G.; Chen, L., Novel Design Concepts of Efficient Mg-Ion Electrolytes toward High-Performance Magnesium–Selenium and Magnesium–Sulfur Batteries. *Adv. Energy Mater.* **2017,** *7*, 1602055.

60.   Tutusaus, O.; Mohtadi, R.; Arthur, T. S.; Mizuno, F.; Nelson, E. G.; Sevryugina, Y. V., An Efficient Halogen-Free Electrolyte for Use in Rechargeable Magnesium Batteries. *Angew. Chem. Int. Ed.* **2015,** *54*, 7900-7904.

61.   Zhao-Karger, Z.; Zhao, X.; Wang, D.; Diemant, T.; Behm, R. J.; Fichtner, M., Performance Improvement of Magnesium Sulfur Batteries with Modified Non-Nucleophilic Electrolytes. *Adv. Energy Mater.* **2015,** *5*, 1401155.

62.   Muldoon, J.; Bucur, C. B.; Gregory, T., Fervent Hype behind Magnesium Batteries: An Open Call to Synthetic Chemists—Electrolytes and Cathodes Needed. *Angew. Chem. Int. Ed.* **2017,** *56*, 12064-12084.

63.   Huie, M. M.; Bock, D. C.; Takeuchi, E. S.; Marschilok, A. C.; Takeuchi, K. J., Cathode Materials for Magnesium and Magnesium-Ion Based Batteries. *Coord. Chem. Rev.* **2015,** *287*, 15-27.

64.   Saha, P.; Datta, M. K.; Velikokhatnyi, O. I.; Manivannan, A.; Alman, D.; Kumta, P. N., Rechargeable Magnesium Battery: Current Status and Key Challenges for the Future. *Prog. Mater. Sci.* **2014,** *66*, 1-86.

65.   Zhou, B.; Shi, H.; Cao, R.; Zhang, X.; Jiang, Z., Theoretical Study on the Initial Stage of a Magnesium Battery Based on a V_2O_5 Cathode. *Phys. Chem. Chem. Phys.* **2014,** *16*, 18578-18585.

66.   Jiao, L.; Yuan, H.; Wang, Y.; Cao, J.; Wang, Y., Mg Intercalation Properties Into Open-Ended Vanadium Oxide Nanotubes. *Electrochem. Commun.* **2005,** *7*, 431-436.

67.   Nam, K. W.; Kim, S.; Lee, S.; Salama, M.; Shterenberg, I.; Gofer, Y.; Kim, J.-S.; Yang, E.; Park, C. S.; Kim, J.-S.; Lee, S.-S.; Chang, W.-S.; Doo, S.-G.; Jo, Y. N.; Jung, Y.; Aurbach, D.; Choi, J. W., The High Performance of Crystal Water Containing Manganese Birnessite Cathodes for Magnesium Batteries. *Nano Lett.* **2015,** *15*, 4071-4079.

68.   Kim, C.; Phillips, P. J.; Key, B.; Yi, T.; Nordlund, D.; Yu, Y.-S.; Bayliss, R. D.; Han, S.-D.; He, M.; Zhang, Z.; Burrell, A. K.; Klie, R. F.; Cabana, J., Direct Observation of Reversible Magnesium Ion Intercalation into a Spinel Oxide Host. *Adv. Mater.* **2015,** *27*, 3377-3384.

69.   Wang, R. Y.; Wessells, C. D.; Huggins, R. A.; Cui, Y., Highly Reversible Open Framework Nanoscale Electrodes for Divalent Ion Batteries. *Nano Lett.* **2013,** *13*, 5748-5752.

70.   Gershinsky, G.; Yoo, H. D.; Gofer, Y.; Aurbach, D., Electrochemical and Spectroscopic Analysis of Mg^{2+} Intercalation into Thin Film Electrodes of Layered Oxides: V_2O_5 and MoO_3. *Langmuir* **2013,** *29*, 10964-10972.

71.   Liu, B.; Luo, T.; Mu, G.; Wang, X.; Chen, D.; Shen, G., Rechargeable Mg-Ion Batteries Based on WSe_2 Nanowire Cathodes. *ACS Nano* **2013,** *7*, 8051-8058.

72.   NuLi, Y.; Zheng, Y.; Wang, F.; Yang, J.; Minett, A. I.; Wang, J.; Chen, J., MWNT/C/$Mg_{1.03}Mn_{0.97}SiO_4$ Hierarchical Nanostructure for Superior Reversible Magnesium Ion Storage. *Electrochem. Commun.* **2011,** *13*, 1143-1146.

73.   Rasul, S.; Suzuki, S.; Yamaguchi, S.; Miyayama, M., Synthesis and Electrochemical Behavior of Hollandite MnO_2/Acetylene Black Composite Cathode for Secondary Mg-Ion Batteries. *Solid State Ionics* **2012,** *225*, 542-546.

74.   Lee, S. H.; DiLeo, R. A.; Marschilok, A. C.; Takeuchi, K. J.; Takeuchi, E. S., Sol Gel Based Synthesis and Electrochemistry of Magnesium Vanadium Oxide: A Promising Cathode Material for Secondary Magnesium Ion Batteries. *ECS Electrochem. Lett.* **2014,** *3*, A87-A90.

75.   Tutusaus, O.; Mohtadi, R., Paving the Way towards Highly Stable and Practical Electrolytes for Rechargeable Magnesium Batteries. *ChemElectroChem* **2014,** *2*, 51-57.

76.   Sun, X.; Bonnick, P.; Nazar, L. F., Layered TiS_2 Positive Electrode for Mg Batteries. *ACS Energy Lett.* **2016,** *1*, 297-301.

77.   Tashiro, Y.; Taniguchi, K.; Miyasaka, H., The Effect of Anion-sublattice Structure on the Displacement Reaction in Copper Sulfide Cathodes of Rechargeable Magnesium Batteries. *Chem. Lett.* **2017,** *46*, 1240-1242.

78.   Huie, M. M.; Bock, D. C.; Takeuchi, E. S.; Marschilok, A. C.; Takeuchi, K. J., Cathode Materials for Magnesium and Magnesium-Ion Based Batteries. *Coord. Chem. Rev.* **2015,** *287*, 15-27.

79.   Sun, X.; Bonnick, P.; Duffort, V.; Liu, M.; Rong, Z.; Persson, K. A.; Ceder, G.; Nazar, L. F., A High Capacity Thiospinel Cathode for Mg Batteries. *Energy Environ. Sci.* **2016,** *9*, 2273-2277.

80.   Arsentev, M.; Missyul, A.; Petrov, A. V.; Hammouri, M., TiS_3 Magnesium Battery Material: Atomic-Scale Study of Maximum Capacity and Structural Behavior. *J. Phys. Chem. C* **2017,** *121*, 15509-15515.

81.   Xiong, F.; Fan, Y.; Tan, S.; Zhou, L.; Xu, Y.; Pei, C.; An, Q.; Mai, L., Magnesium Storage Performance and Mechanism of CuS Cathode. *Nano Energy* **2018,** *47*, 210-216.

82.   Vinayan, B. P.; Zhao-Karger, Z.; Diemant, T.; Chakravadhanula, V. S. K.; Schwarzburger, N. I.; Cambaz, M. A.; Behm, R. J.; Kubel, C.; Fichtner, M., Performance Study of Magnesium-Sulfur Battery Using a Graphene Based Sulfur Composite Cathode Electrode and a Non-nucleophilic Mg Electrolyte. *Nanoscale* **2016,** *8*, 3296-3306.

83.   Lossius, L. P.; Emmenegger, F., Plating of Magnesium From Organic Solvents. *Electrochim. Acta* **1996,** *41*, 445-447.

84.   Shao, Y.; Gu, M.; Li, X.; Nie, Z.; Zuo, P.; Li, G.; Liu, T.; Xiao, J.; Cheng, Y.; Wang, C.; Zhang, J.-G.; Liu, J., Highly Reversible Mg Insertion in Nanostructured Bi for Mg Ion Batteries. *Nano Lett.* **2013,** *14*, 255-260.

85.   Murgia, F.; Stievano, L.; Monconduit, L.; Berthelot, R., Insight Into the Electrochemical Behavior of Micrometric Bi and Mg_3Bi_2 as High Performance Negative Electrodes for Mg Batteries. *J. Mater. Chem. A* **2015,** *3*, 16478-16485.

86.   Arthur, T. S.; Singh, N.; Matsui, M., Electrodeposited Bi, Sb and $Bi_{1-x}Sb_x$ Alloys as Anodes for Mg-Ion Batteries. *Electrochem. Commun.* **2012,** *16*, 103-106.

87.   Liu, Z.; Lee, J.; Xiang, G.; Glass, H. F. J.; Keyzer, E. N.; Dutton, S. E.; Grey, C. P., Insights Into the Electrochemical Performances of Bi Anodes for Mg Ion Batteries Using ^{25}Mg Solid State NMR Spectroscopy. *Chem. Commun.* **2017,** *53*, 743-746.

88.   Sedighi, M.; Arghavani Nia, B.; Zarringhalam, H.; Moradian, R., Density Functional Theory Study of the Structural and Electronic Properties of Mg_3Bi_2 in Hexagonal and Cubic Phases. *Eur. Phys. J. Appl. Phys.* **2013,** *61*, 10103.

89.   Jin, W.; Li, Z.; Wang, Z.; Fu, Y. Q., Mg Ion Dynamics in Anode Materials of Sn and Bi for Mg-Ion Batteries. *Mater. Chem. Phys.* **2016,** *182*, 167-172.

90.   Benmayza, A.; Ramanathan, M.; Singh, N.; Mizuno, F.; Prakash, J., Electrochemical and Thermal Studies of Bismuth Electrodes for Magnesium-Ion Cells. *J. Electrochem. Soc.* **2015,** *162*, A1630-A1635.

91.   Ramanathan, M.; Benmayza, A.; Prakash, J.; Singh, N.; Mizuno, F., A Porous Electrode Model for the Magnesiation and Demagnesiation of a Bismuth Electrode in Rechargeable Magnesium-Ion Cells. *J. Electrochem. Soc.* **2016,** *163*, A477-A487.

92.   DiLeo, R. A.; Zhang, Q.; Marschilok, A. C.; Takeuchi, K. J.; Takeuchi, E. S., Composite Anodes for Secondary Magnesium Ion Batteries Prepared *via* Electrodeposition of Nanostructured Bismuth on Carbon Nanotube Substrates. *ECS Electrochem. Lett.* **2015,** *4*, A10-A14.

93.   Wang, W.; Liu, L.; Wang, P.-F.; Zuo, T.-T.; Yin, Y.-X.; Wu, N.; Zhou, J.-M.; Wei, Y.; Guo, Y.-G., A Novel Bismuth-Based Anode Material with a Stable Alloying Process by the Space Confinement of an *In Situ* Conversion Reaction for a Rechargeable Magnesium Ion Battery. *Chem. Commun.* **2018,** *54*, 1714-1717.

94.   Penki, T. R.; Valurouthu, G.; Shivakumara, S.; Sethuraman, V. A.; Munichandraiah, N., *In Situ* Synthesis of Bismuth (Bi)/Reduced Graphene Oxide (RGO) Nanocomposites as High-Capacity Anode Materials for a Mg-Ion Battery. *New J. Chem.* **2018,** *42*, 5996-6004.

95.   Singh, N.; Arthur, T. S.; Ling, C.; Matsui, M.; Mizuno, F., A high Energy-Density Tin Anode for Rechargeable Magnesium-Ion Batteries. *Chem. Commun.* **2013,** *49*, 149-151.

96.   Nguyen, D. T.; Tran, X. M.; Kang, J.; Song, S. W., Magnesium Storage Performance and Surface Film Formation Behavior of Tin Anode Material. *ChemElectroChem* **2016,** *3*, 1813-1819.

97.   Periyapperuma, K.; Tran, T. T.; Purcell, M. I.; Obrovac, M. N., The Reversible Magnesiation of Pb. *Electrochim. Acta* **2015,** *165*, 162-165.

98.   Murgia, F.; Weldekidan, E. T.; Stievano, L.; Monconduit, L.; Berthelot, R., First Investigation of Indium-Based Electrode in Mg Battery. *Electrochem. Commun.* **2015,** *60*, 56-59.

99.   Murgia, F.; Laurencin, D.; Weldekidan, E. T.; Stievano, L.; Monconduit, L.; Doublet, M.-L.; Berthelot, R., Electrochemical Mg Alloying Properties Along the $Sb_{1-x}Bi_x$ Solid Solution. *Electrochim. Acta* **2018,** *259*, 276-283.

100.   Murgia, F.; Monconduit, L.; Stievano, L.; Berthelot, R., Electrochemical Magnesiation of the Intermetallic InBi Through Conversion-Alloying Mechanism. *Electrochim. Acta* **2016,** *209*, 730-736.

101.   Parent, L. R.; Cheng, Y.; Sushko, P. V.; Shao, Y.; Liu, J.; Wang, C.-M.; Browning, N. D., Realizing the Full Potential of Insertion Anodes for Mg-Ion Batteries Through the Nanostructuring of Sn. *Nano Lett.* **2015,** *15*, 1177-1182.

102.   Yingwen, C.; Yuyan, S.; R., P. L.; L., S. M.; Guosheng, L.; V., S. P.; D., B. N.; Chongmin, W.; Jun, L., Interface Promoted Reversible Mg Insertion in Nanostructured Tin–Antimony Alloys. *Adv. Mater.* **2015,** *27*, 6598-6605.

103.   Nayeb-Hashemi, A. A.; Clark, J. B., The Bi-Mg (Bismuth-Magnesium) System. *Bull. Alloy Phase Diagrams* **1985,** *6*, 528-533.

104.   Barnes, A. C.; Guo, C.; Howells, W. S., Fast-Ion Conduction and the Structure of β-Mg_3Bi_2. *J. Phys.: Condens. Matter* **1994,** *6*, L467-L471.

105.   He, M.; Protesescu, L.; Caputo, R.; Krumeich, F.; Kovalenko, M. V., A General Synthesis Strategy for Monodisperse Metallic and Metalloid Nanoparticles (In, Ga, Bi, Sb, Zn, Cu, Sn, and Their Alloys) *via In Situ* Formed Metal Long-Chain Amides. *Chem. Mater.* **2015,** *27*, 635-647.

106.   Law, M.; Luther, J. M.; Song, Q.; Hughes, B. K.; Perkins, C. L.; Nozik, A. J., Structural, Optical, and Electrical Properties of PbSe Nanocrystal Solids Treated Thermally or with Simple Amines. *J. Am. Chem. Soc.* **2008,** *130*, 5974-5985.

107.   Talapin, D. V.; Murray, C. B., PbSe Nanocrystal Solids for n- and p-Channel Thin Film Field-Effect Transistors. *Science* **2005,** *310*, 86-89.

108.   Zhang, H.; Hu, B.; Sun, L.; Hovden, R.; Wise, F. W.; Muller, D. A.; Robinson, R. D., Surfactant Ligand Removal and Rational Fabrication of Inorganically Connected Quantum Dots. *Nano Lett.* **2011,** *11*, 5356-5361.

109.   Prehal, C.; Weingarth, D.; Perre, E.; Lechner, R. T.; Amenitsch, H.; Paris, O.; Presser, V., Tracking the Structural Arrangement of Ions in Carbon Supercapacitor Nanopores using *In Situ* Small-Angle X-ray Scattering. *Energy Environ. Sci.* **2015,** *8*, 1725-1735.

110.   Rieker, T. P.; Hindermann-Bischoff, M.; Ehrburger-Dolle, F., Small-Angle X-ray Scattering Study of the Morphology of Carbon Black Mass Fractal Aggregates in Polymeric Composites. *Langmuir* **2000,** *16*, 5588-5592.

111.   Glatter, O.; Kratky, O., *Editors. Small-Angle X-ray Scattering*. New York: Academic Press: 1982.

112.   Lancry, E.; Levi, E.; Mitelman, A.; Malovany, S.; Aurbach, D., Molten Salt Synthesis (MSS) of $Cu_2Mo_6S_8$—New Way for Large-scale Production of Chevrel Phases. *J. Solid State Chem.* **2006,** *179*, 1879-1882.

113.   Perdew, J. P.; Zunger, A., Self-Interaction Correction to Density-Functional Approximations for Many-Electron Systems. *Phys. Rev. B* **1981,** *23*, 5048-5079.

114.   Ceperley, D.; Alder, B. J., Ground State of the Electron Gas by a Stochastic Method. *Phys. Rev. Lett.* **1980,** *45*, 566-569

TOC Graphics: